

Lab on a Chip

Accepted Manuscript

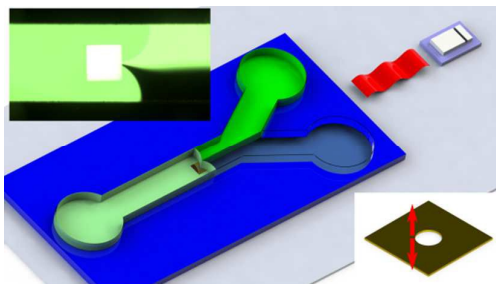


This is an *Accepted Manuscript*, which has been through the Royal Society of Chemistry peer review process and has been accepted for publication.

Accepted Manuscripts are published online shortly after acceptance, before technical editing, formatting and proof reading. Using this free service, authors can make their results available to the community, in citable form, before we publish the edited article. We will replace this *Accepted Manuscript* with the edited and formatted *Advance Article* as soon as it is available.

You can find more information about *Accepted Manuscripts* in the [Information for Authors](#).

Please note that technical editing may introduce minor changes to the text and/or graphics, which may alter content. The journal's standard [Terms & Conditions](#) and the [Ethical guidelines](#) still apply. In no event shall the Royal Society of Chemistry be held responsible for any errors or omissions in this *Accepted Manuscript* or any consequences arising from the use of any information it contains.



A vibrating membrane with discontinuities in the form of through holes is utilised to achieve millisecond mixing.

Vibrating membrane with discontinuities for rapid and efficient microfluidic mixing[†]

Hoang Van Phan,^a M. Bulut Coşkun,^a Muhsincan Şeşen,^a Gregory Pandraud,^b Adrian Neild^a and Tuncay Alan^{a*}

Received Xth XXXXXXXXXXXX 20XX, Accepted Xth XXXXXXXXXXXX 20XX

First published on the web Xth XXXXXXXXXXXX 200X

DOI: 10.1039/b000000x

This study presents a novel acoustic mixer comprising of a microfabricated silicon nitride membrane with a hole etched through it. We show that the introduction of the through hole leads to extremely fast and homogeneous mixing. When the membrane is immersed in fluid and subjected to acoustic excitation, a strong streaming field in the form of vortices is generated. The vortices are always observed to centre at the hole, pointing to the critical role it has on the streaming field. We hypothesise that the hole introduces a discontinuity to the boundary conditions of the membrane, leading to strong streaming vortices. With numerical simulations, we show that the hole's presence can increase the volume force responsible for driving the streaming field by 2 orders of magnitude, thus supporting our hypothesis. We investigate the mixing performance at different Peclet numbers by varying the flow rates for various devices containing circular, square and rectangular shaped holes of different dimensions. We demonstrate rapid mixing within 3 ms mixing time (90% mixing efficiency at 60 $\mu\text{l}/\text{min}$ total flow rate, Peclet number equals $8333 \pm 3.5\%$) is possible with the current designs. Finally, we examine the membrane with two circular holes which are covered by air bubbles and compare it to when the membrane is fully immersed. We find that coupling between the holes' vortices occurs only when membrane is immersed; while with the bubble membrane, the upstream hole's vortices can act as a blockage to fluid flow passing it.

1 Introduction

Efficient, homogeneous mixing of fluids is crucial for a variety of microfluidic applications ranging from complex chemical reactions¹ and protein studies² to nanoparticle synthesis.^{3–5} However, fluid flows at micro and nano scales usually lie in the laminar regime, which is characterised by a low Reynolds number ($Re = \rho UL/\mu \ll 100$, where ρ is the fluid density, U is the flow velocity, L is the characteristic length and μ is the fluid's dynamic viscosity). Consequently, in the absence of external influences, mixing at this scale is dominated by diffusion, a prohibitively long process.⁶

To simultaneously reduce the mixing time and increase the mixing efficiency (i.e. how homogeneously fluids are mixed) in microfluidic channels, many enhancement strategies have been investigated. Broadly, they can be divided into two categories: passive^{7–11} and active methods.^{12–17} Each group has its own advantages and limitations in terms of effectiveness, mixing time, control and ease of operation. Since passive mix-

ers (such as the chaotic mixer⁸ and the hydrodynamic focusing mixer⁷) do not require any external devices nor a power source, they are extremely simple to operate and integrate with different applications. However, they are usually outperformed by their active counterparts with respect to mixing efficiency and time.^{18,19} Furthermore, the required channel length of passive mixers can compromise the appealing compactness of microfluidic systems.

Acoustic mixers offer significant advantages for rapid mixing. Firstly, they do not impose any limitations on the working fluid medium such as conductivity¹⁴ or requirement of magnetic particle suspensions.¹⁵ Secondly, acoustic energy can safely be used in various biological and chemical applications. Thirdly, acoustofluidics is a strong, mature and thriving field with many demonstrated capabilities such as particle manipulation^{20–26} and, of course, mixing.^{13,27–33}

An acoustic mixer's operation depends on the resonance of vibrating features to perturb the steady flow to induce mixing. A compelling example of this approach is an air bubble trapped in a microfluidic channel.^{13,29} The actuation of a microbubble results in a streaming field in the form of vortices due to the oscillatory boundary. Compared to pressure fluctuations from other types of ultrasonic transducers, these vortices disturb the flow more strongly^{34,35} and rapidly. (In comparison, the fluids need to travel for more than 4 mm to be mixed

^aLaboratory for Micro Systems, Department of Mechanical and Aerospace Engineering, Monash University, Clayton, VIC 3800, Australia.

Email: tuncay.alan@monash.edu. Tel: +61 3 990 53709.

^bElse Kooi Laboratory, Delft University of Technology 2628 CT Delft, The Netherlands

[†] Electronic Supplementary Information (ESI) available: Videos of flow visualisation and the best membrane mixer. See DOI: 10.1039/b000000x/

completely using integrated digital transducers.³¹) Nevertheless, the primary control parameter of a bubble mixer is its radius, thus even a slight disturbance to the bubble's shape can affect the resonant frequency.³² Furthermore, bubble instability can arise from changes in flow pressure and heating. Oscillating sharp-edges can overcome the bubble instability problem in exchange for weaker flow disturbances.³² An ideal design should be able to generate significant disturbances, have a well-defined stable frequency and provide easy control.

Here we present a novel approach, the acoustic membrane, that utilises silicon nitride (SiN) membranes containing specially designed microfabricated features for efficient mixing. Under acoustic excitations, the membrane generates a vortical acoustic streaming field that is inherently different from that of a bubble: the vortices' plane is perpendicular to the direction of the membrane's transverse vibrations and the contingent presence of the hole. In contrast to a continuous membrane without a hole, these steady streaming fields are significantly stronger, leading to extremely good mixing performance comparable to that of a bubble mixer, but with the added advantage of precise control throughout operation. The complexity of the observed vortices points to an intricate fluid-structure interaction problem. We hypothesise that the hole's presence gives rise to a discontinuity to the otherwise continuous boundary conditions on the membrane surface. This is supported by numerical simulations that show how the body force field, which is responsible for inducing streaming, changes with the inclusion of the through hole. We also investigate the mixing performance at different flow rates for various geometries such as circular, square and rectangular. Most notably, we show that homogeneous mixing is possible at 60 $\mu\text{l}/\text{min}$ (Peclet number $\approx 8333 \pm 3.5\%$) with 3 ms mixing time. And lastly, we show how having an air/liquid interface blocking the membrane's holes can affect the streaming pattern.

2 Methodology

2.1 Fabrication and experimental set-up

The device comprises of a Y-shaped microfluidic channel made from polydimethyl siloxane (PDMS) bonded on a SiN chip containing the membranes (Fig. 1(a)). The fabrication processes for both the membrane and the channel are summarised in Fig. 1(e). For the membranes, firstly, the backside openings and front-side geometric features are patterned on 1- μm -thick SiN coated (100)-oriented Si wafers (4D LABS, Canada) through photolithography and reactive ion etching (RIE). The wafers are then immersed in a 5M KOH solution at 65°C for approximately 15 hours to selectively etch the Si and release the SiN membranes. The wafers are then scribed into small chips, each containing a 1- μm -thick SiN membrane with width a ranging from 210 to 475 μm . Importantly,

the membranes contain through holes of varying shapes, with characteristic lengths denoted by d . The membrane fabrication steps were inspired by similar designs employed in specialised transmission electron microscopy (TEM) grids.^{36–38}

The PDMS channels are fabricated using standard procedures. The features are patterned on a (100) Si wafer, which is then etched by deep reactive ion etching (DRIE). The surface is rendered hydrophobic by a layer of teflon coating. PDMS is mixed with curing agent (SYLGARD[®] 184, Dow Corning) at ratio 10:1 w/w, and then casted on the mould. The mixture is left in a vacuum pump for 2 hours, and then on a hot plate at 65°C for complete curing. Finally, the PDMS channel is peeled off, cut and bonded onto the chip containing the membranes. The channel width W ranges from 750 to 1000 μm , and the height H varies between 70 to 86 μm .

After assembly, the entire structure is adhered together with the bottom outlet (Cole-Parmer[®] thin wall tubing) to a glass slide using epoxy (Selleys[®] Araldite[®]). The device is excited by a piezoelectric disk (Ferroperm Piezoceramics), which is also bonded on the glass slide with epoxy. To initialise the system, water is pumped through the channel while ensuring that it also exits through the bottom outlet (the membrane must be completely immersed). After this step, the outlet is blocked so that the fluid only flows over the membrane. Water with and without fluorescent dye (Invitrogen[™] Molecular Probes[™]) is injected into each of the two inlets by means of a syringe pump (kdScientific KDS-101-CE). The flow rates of both streams are kept equal, and their total flow rate Q is chosen to be 10, 20, 40, 60 and 80 $\mu\text{l}/\text{min}$ unless otherwise stated. The PZT is driven by a signal generator (Stanford Research Systems DS345) and an amplifier (T&C Power Conversion, Inc. AG 1006) at 200 V_{pp} . The membrane's resonant frequency is found experimentally by frequency sweeping. Flow visualisation is performed with 2.01 μm fluorescent particles (Bangs Laboratories, Inc.[™]) suspended in a water solution with 2 wt% PEG (CAS: 9003-11-6, Sigma-Aldrich). All experiments are recorded by a PixelINK camera at 15 frames per second.

2.2 Data analysis

The effects of varying the total flow rate and different PDMS channel's dimensions are captured by the dimensionless Peclet number Pe :

$$Pe = \frac{UL}{D} \quad (1)$$

where U is the average flow velocity, L the characteristic length and D the diffusion coefficient of the fluorescent dye. (We use $D = 1.5 \times 10^{-3} \text{ m}^2/\text{s}$ in the calculations.³⁹)

Next, to quantify how good mixing is, we first analyse the fluorescence intensity of the recorded videos. After each frame is converted into grayscale (and rotated as necessary to

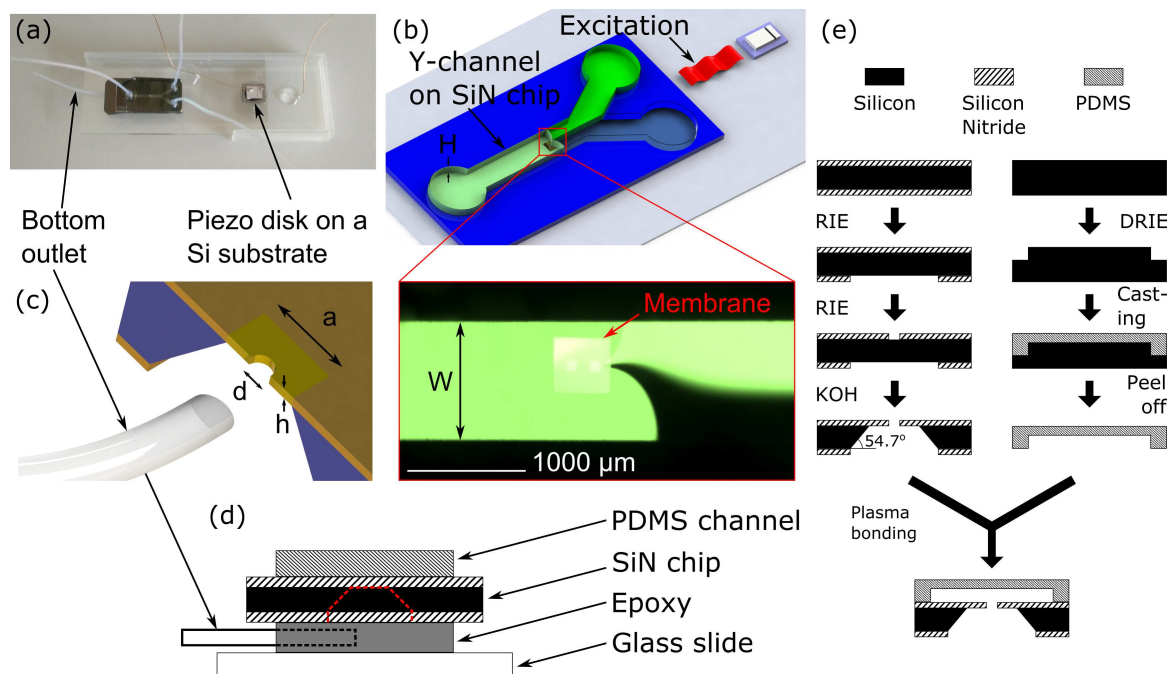


Fig. 1 (a) Photograph of the microfluidic device. (b) Schematic of the acoustic membrane mixer. (W and H denote the PDMS channel's width and height.) (c) The cross-section of the membrane together with the bottom outlet. (a , d and h denote the membrane's side length, hole size and thickness respectively.) (d) Simplified side view of the microfluidic device, showing how the bottom outlet is placed beneath the SiN chip. (e) Fabrication process of the SiN chip and the PDMS channel. The Si layer is etched anisotropically at 54.7° from the (100) (i.e. horizontal) plane.

ensure that the channel is horizontal), the channel walls are identified using MATLAB's built-in edge detection function 'edge'. The mixed and unmixed regions are chosen randomly downstream and upstream respectively (Fig 2a), from which the intensities are obtained. An example of this choice and the edge detection image are shown in Fig. 2(a) and (b), and the corresponding intensity in grayscale is given in Fig. 2(c). The intensities are then used to calculate the mixing index MI :⁴⁰

$$MI = 1 - \frac{\sqrt{\frac{1}{N} \sum_{i=1}^N (I_i - \bar{I})^2}}{\sqrt{\frac{1}{N} \sum_{i=1}^N (I'_i - \bar{I}')^2}}, \quad (2)$$

where N is the number of pixels of each region, I_i and \bar{I} denotes the local raw intensity of the i -th pixel and the average raw intensity of the mixed region respectively, and (\prime) denotes the intensity of the unmixed region. (MI being closer to 1 implies mixing is more uniform.) This particular formula for MI is chosen among the others as it was shown to be the least affected by lighting conditions and microscopes.⁴⁰

In addition to homogeneity, it is also of great interest to determine how fast the fluids are mixed. The mixing time t_{mix} is estimated by the common methods reported in literature for

acoustic mixers:^{29,30,32}

$$t_{mix} = L_{mix}/U, \quad (3)$$

where L_{mix} is the calculated mixing length based on the assumed transition length and $U = Q/WH$ is the average flow velocity in the channel. Faster mixing time has important implications in applications of microfluidic mixing, such as higher monodispersity for synthesis of lipid nanoparticles.⁴ To approximate L_{mix} , firstly, a step function in the form of $y = C_1 + C_2/(1 + e^{-C_3(x-C_4)})$, where C_i are constant coefficients, is fitted to the normalised intensity of the chosen transition length. The cut-off intensities are equal to 2% of the maximum value of the fitted curve above and below the minimum and maximum of said curve, respectively. These two values dictate L_{mix} in pixels, which is then converted into μm by scaling it with the channel's width.

To quantify the uncertainty in the analysis process, we analyse and average the data across 15 frames (i.e. one full second in real-time). The error bar is estimated by one standard error of these 15 data sets.

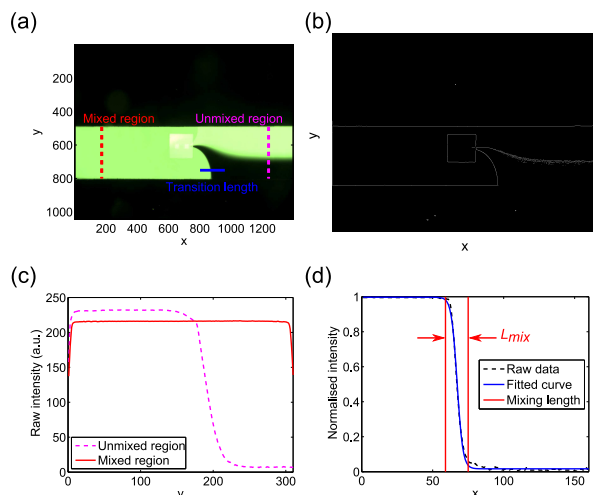


Fig. 2 (a) An example of the location chosen for intensity analysis and the transition length for mixing time calculation. (b) Edge detection using MATLAB's built-in function `edge` with 'Canny' option. (c) Raw intensity (arbitrary units) of the mixed and unmixed region. (d) The normalised intensity (to range between 0 and 1) of the transition length, the fitted step function and the identified mixing transition length. All x-axes are in pixels. For this example, $MI = 0.92$ and $t_{mix} = 25$ ms.

2.3 Numerical simulation

We hypothesise that firstly, a continuous (i.e. holeless) membrane can generate a streaming field, albeit a weak one, as is the case for a vibrating bubble or a flexural plate wave.⁴¹ Secondly, the hole introduces a discontinuity to the boundary conditions at its perimeter, leading to a higher velocity gradient, especially within the Stokes' boundary layer. And finally, this gradient results in a strong volume force field that is responsible for the observed microstreaming vortices. The hypothesis is supported by numerical simulations and experimental results.

Assume a fluid volume that is being disturbed by vibrating structures/surfaces (for example, a vibrating air/water interface). Applying the perturbation method on the fluid's pressure field, p , the velocity field, \mathbf{v} , and the fluid's density, ρ , yields:

$$p = p_0 + \varepsilon p_1 + \varepsilon^2 p_2 \quad (4a)$$

$$\mathbf{v} = \mathbf{v}_0 + \varepsilon \mathbf{v}_1 + \varepsilon^2 \mathbf{v}_2 \quad (4b)$$

$$\rho = \rho_0 + \varepsilon \rho_1 \quad (4c)$$

where ε is a small perturbation and subscripts 0, 1 and 2 denote the unperturbed, first-order and second-order value, respectively. The acoustic streaming (steady microstreaming) pattern that is experimentally observed is the time-averaged second-order velocity field: $\mathbf{v}_s = \langle \mathbf{v}_2 \rangle$. Note that $\langle \rangle$ denotes the time-average operator.

There are generally two ways to find \mathbf{v}_s : (i) we can directly solve the time-dependent Navier-Stokes equation while forcing the velocity field at the membrane surface to be equal to the membrane's vibration, or (ii) we first find the first-order velocity field to calculate the body force \mathbf{F} that drives the streaming field:^{42,43}

$$\mathbf{F} = -\rho_0 \langle (\mathbf{v}_1 \cdot \nabla) \mathbf{v}_1 + \mathbf{v}_1 (\nabla \cdot \mathbf{v}_1) \rangle \quad (5)$$

The force field is then used as the input to the steady-state compressible Navier-Stokes equation (with appropriate boundary conditions):

$$\rho_0 (\mathbf{v}_s \cdot \nabla) \mathbf{v}_s = -\nabla p_2 + \mu \nabla^2 \mathbf{v}_s + (\mu_B + \frac{1}{3} \mu) \nabla (\nabla \cdot \mathbf{v}_s) + \mathbf{F} \quad (6)$$

where μ and μ_B is the dynamic and bulk viscosity of fluid, respectively.

The first-order velocity field \mathbf{v}_1 itself can be obtained by two methods:

1. The first-order pressure field p_1 is found from the viscous Helmholtz equation. Then, \mathbf{v}_1 is calculated as $\mathbf{v}_1 = -\nabla p_1 / i\omega\rho$ (ω : excitation angular frequency, ρ : fluid's density, and i : the imaginary unit).⁴⁴
2. \mathbf{v}_1 can be solved directly from the perturbation equations for the thermoacoustics fields.^{45,46}

Importantly, if one employs method 1, the body force \mathbf{F} must be corrected by an exponential decay function.^{42,44} This is necessary to take into account the effects of the no-slip condition at the walls and the viscous boundary layer (Stokes' layer), the thickness of which is given by:

$$\delta = \sqrt{\frac{2\mu}{\omega\rho_0}} \quad (7)$$

where ω is the excitation angular frequency. At a typical excitation frequency of 150 kHz, $\delta = 1.378 \mu\text{m}$.

Computationally, solving the time-dependent Navier-Stokes equations is more time-consuming than the method of calculating the body force from the first-order velocity field. This is because once \mathbf{v}_1 is obtained, only the stationary Navier-Stokes equation need be solved. And even for finding \mathbf{v}_1 , approach 1 (solving the Helmholtz equations) is significantly more computationally efficient because it need only solve for one variable, the pressure field, and gives a reasonably accurate approximation provided that the correct decay function is chosen.

The right decay function can prove challenging to find, especially for the cases with complicated geometries such as the singularity at the through hole's edges. The thermoacoustics approach, on the other hand, allows for the correct body force to be calculated directly from \mathbf{v}_1 without needing any modifications, regardless of the geometry. The downside is that it is

more computationally expensive than method 1: the unknown variables are both p_1 and \mathbf{v}_1 , plus the first-order temperature field T_1 :

$$T = T_0 + \varepsilon T_1 + \varepsilon^2 T_2 \quad (8)$$

The thermoacoustics equations also involves an important parameter, the thermal boundary layer thickness:

$$\delta_{th} = \sqrt{\frac{2D_{th}}{\omega}} \quad (9)$$

where D_{th} is fluid's thermal diffusivity. At 150 kHz, $\delta_{th} = 0.551 \mu\text{m}$. The temperature field changes rapidly within this thermal boundary layer.

In this study, method 2 (solving the thermoacoustics equations) is chosen to model the membrane. COMSOL Multiphysics 5.0 is used to solve for the first-order fields (p_1 , \mathbf{v}_1 , and T_1) with its Thermoacoustics Module. Only the 2D cross-section of the channel and the membrane is simulated. (We will discuss the reasons for only performing a 2D simulation later.) All water's properties used in the model are given in the ESI.

To show that the presence of the hole can significantly enhance mixing, we model both a $420\text{-}\mu\text{m}$ -wide membrane with and without a $100\text{-}\mu\text{m}$ -diameter circular hole. The boundary conditions (BC) are:

$$T_1 = 0, \text{ on all walls} \quad (10a)$$

$$\mathbf{v}_1 = \mathbf{0}, \text{ on all walls, except} \quad (10b)$$

$$\mathbf{v}_1 = 0\mathbf{e}_x + U_0 w(x)\mathbf{e}_y, \text{ on membrane's surface} \quad (10c)$$

where U_0 is the velocity amplitude, $w(x)$ is the membrane's deflection shape, \mathbf{e}_x and \mathbf{e}_y are the unit vectors in x and y -directions respectively. The mechanical BCs and device dimensions are given in Fig. 3 (see the last picture in Fig. 1(e) to visualise the modelled cross-section). To reduce the memory requirement, the symmetry of the system is utilised, the pressure and velocity fields are computed segregatedly from the temperature field, and the fluid in the cavity below the membrane is truncated at $150 \mu\text{m}$ (instead of having the full $500\text{-}\mu\text{m}$ -high cavity with a "No-slip" condition at the bottom wall) by the "No stress" condition implemented by COMSOL:

$$\begin{aligned} & \left[-p_1 \mathbf{I} + \mu (\nabla \mathbf{v}_1 + (\nabla \mathbf{v}_1)^T) \right. \\ & \left. - \left(\frac{2}{3} \mu - \mu_B \right) (\nabla \cdot \mathbf{v}_1) \mathbf{I} \right] \mathbf{n} = 0 \end{aligned} \quad (11)$$

where \mathbf{I} is the identity matrix, \mathbf{n} is the outward pointing surface normal vector, and $()^T$ denotes the matrix transpose operator. This condition forces the total surface stress to be zero. (The isothermal condition need not be set on this wall.)

With regards to the "Velocity" BC, we first need to find the deflection shape $w(x)$. For simplicity, we assume that $w(x)$ is

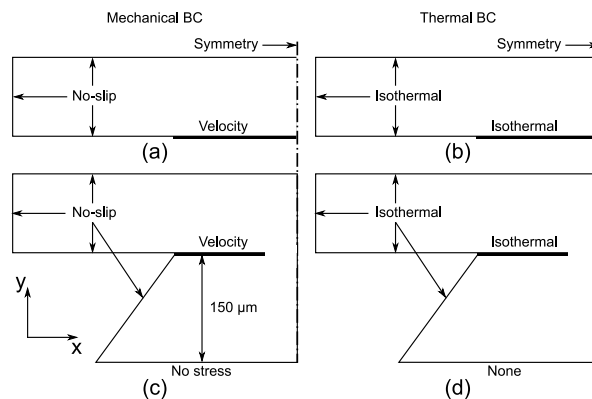


Fig. 3 Boundary conditions for the two types of membrane as set in COMSOL. (a) and (b) show the mechanical and thermal BC of the continuous. (c) and (d) show the mechanical and thermal BC of the membrane with the hole. The bold black lines represent the membrane. The "Velocity" mechanical BC is set according to Eq. (10c). The channel's dimensions are $W = 750 \mu\text{m}$ and $H = 70 \mu\text{m}$, the membrane's dimensions $a = 420 \mu\text{m}$ and $d = 100 \mu\text{m}$.

equal to the fundamental resonance mode shape. For a hole-less membrane, the fixed-fixed beam solution applies:⁴⁷

$$w(x) = \cos k_1(x/a - 0.5) + C \cosh k_1(x/a - 0.5) \quad (12)$$

where $k_1 \approx 4.730$, $C = \sin(k_1/2)/\sinh(k_1/2)$ and a is the membrane side length. For the membrane with hole, the first mode shape is calculated using COMSOL's Plate Physics Module, and a 4th-order polynomial is fitted on the obtained deflection. For the modelled membrane ($a = 420 \mu\text{m}$ and $d = 100 \mu\text{m}$):

$$\begin{aligned} w(x') \approx & 1.529x'^4 - 5.213x'^3 \\ & + 6.318x'^2 + 8.034 \times 10^{-4}x' \end{aligned} \quad (13)$$

where $x' = x/\frac{a-d}{2}$ ($0 \leq x' \leq \frac{a-d}{2}$) is the normalised distance from the fixed edge. (The polynomial has $R^2 \approx 1$.)

The velocity amplitude U_0 is set such that:

$$\int_0^a U_0 w(x) dx = a_0 \omega a \quad (14)$$

where a_0 is the scaling excitation amplitude (arbitrarily chosen to be 1 nm in the simulations).

Because of the small geometry at the hole's edge, a mesh convergence analysis is performed on p_1 , \mathbf{v}_1 and T_1 to ensure the validity of the results. The maximum mesh size in the fluid bulk is set to be 10 times as large as that at the domain's walls: $d_{bulk} = 10d_{mesh}$. The mesh size is varied by changing the ratio δ_{th}/d_{mesh} from 0.25 to 2.75. (The thermal boundary layer thickness is used to scale the mesh because it is the smallest

value compared to the viscous layer thickness and the membrane thickness.) The mesh convergence is quantified by the relative convergence parameter $C(g)$:⁴⁶

$$C(g) = \sqrt{\frac{\int (g - g_{\text{ref}})^2 dx dy}{\int (g_{\text{ref}})^2 dx dy}} \quad (15)$$

where g is the solution for a particular mesh size and g_{ref} is the reference solution. The lower $C(g)$ is, the more “converged” the mesh size is. We choose $\delta_{\text{th}}/d_{\text{mesh}} = 3$ as the reference value, which results in $\approx 1.52 \times 10^6$ degrees of freedom (dofs) and uses up to 10.50GB of RAM.

The physics of the membrane obviously presents a complicated fluid-structure interaction problem. Continuous membrane structures have previously been studied experimentally and theoretically for their applications in fluid pumping,^{41,48} and the membrane-fluid coupling effect has been investigated⁴⁹. However, the presence of the through-hole (not considered in the earlier studies) substantially complicates the problem: fluid loading and damping on both sides of the membrane can change its vibration mode, the fluid on each side can couple to each other, and there is a very strong acoustic streaming, a nonlinear effect.

As a result of the system’s complexity, we have to make some assumptions about the numerical model. Firstly, we neglect the coupling between the fluid motion and the vibration of the membrane. Secondly, a 3D model is needed to find the actual streaming field: it is experimentally observed to be parallel to the membrane’s surface (i.e. perpendicular to the membrane’s transverse vibration). It is not justifiable to find the streaming pattern from a 2D simulation, as it would imply the streaming is on the plane normal to the membrane’s surface. Unfortunately, a 3D model is too costly: the need to include the cavity beneath the membrane would significantly increase the already high number of dofs to be solved. For reference, a 3D symmetrical model of a holeless membrane with $\delta_{\text{th}}/d_{\text{mesh}} = 0.1$ has $\approx 10 \times 10^6$ dofs. Thus, in this study, we will only deal with a two-dimensional approximation that the body force driving the streaming field is substantially stronger with the presence of the hole.

3 Results

3.1 Numerical results

As a first step in the numerical study, we performed a mesh convergence analysis (Fig. 4(a)). Since only the body force is of interest, a maximum mesh size of $\delta_{\text{th}}/d_{\text{mesh}} = 2$ at the walls is sufficiently accurate (all variables have achieved 10^{-4} convergence threshold, except the temperature variation T_1 which has achieved $C(g) = 10^{-3}$). It is noteworthy that to avoid numerical singularities, the edges at the hole are filleted, and the mesh size there is always kept constant.

Fig. 4(b)-(d) show the pressure field p_1 and velocity field v_1 (see ESI for the temperature distribution T_1). Our simulations show that the presence of the hole results in a significant increase in the body force (Fig. 4(e) and (f)). The membrane with through hole can generate a body force of $8.5 \times 10^4 \text{ N/m}^3$, as opposed to an approximate $7 \times 10^2 \text{ N/m}^3$ force without it. For comparison, the gravity body force is close to $1 \times 10^4 \text{ N/m}^3$.

This jump of 2 orders of magnitude supports our hypothesis: the hole’s presence both enhances and complicates the streaming effect. Moreover, the volume force is expected to be concentrated around the hole’s edge (Fig. 4(e)) instead of being spread out along the membrane’s surface (Fig. 4(f)). We can only show the expected increase in strength of the streaming vortices associated with the hole because the vortex patterns are not modelled. (Nevertheless, all experiments confirm that the vortices always centre around the hole for different hole geometries and flow conditions (Fig. 5).)

The actual underlying mechanism of the membrane is of course significantly more complex due to the neglected coupling between the membrane and the fluid, the effects of fluid loading/damping and the coupling between the fluid above and beneath the membrane. However, the discontinuity at the membrane still holds even when the coupling effect is considered.

3.2 Experimental results

3.2.1 Streaming field generated by the acoustic membrane. Fig. 5 shows the strong acoustic streaming field generated by the membrane with the through hole (the hole is presented by the bright blue circle in Fig. 5(a) and (c)). The corresponding vortices induce rapid mixing of the two different fluids as they flow past the membrane (see Video 1 in ESI for flow visualisation in Fig. 5(a)). Both the orientation of the vortices with respect to the flow and the strength of the vortices have a considerable effect in the mixing performance. Considering the former, the mixing homogeneity is best when the vortices are symmetrical about the direction of the flow (Fig. 5(f)). In contrast, when the vortices are symmetrical about the line perpendicular to the flow direction as in the case of the rectangular hole (Fig. 5(e)), mixing performance significantly decreases.

In cases with poor mixing, such as in Fig. 5(c), only a fraction of the entering flow passes through the centre of the vortices pair (which is located at the circular hole). The flow portion next to the channel walls is unaffected by the streaming field, resulting in heterogeneous mixing. Nevertheless, the vortices are evidently strongly influenced by the presence of the hole: they are always centred around it, regardless of the hole geometry (Fig. 5(e) and (f)), or whether the hole is offset from the membrane’s centre or not (Fig. 5(g)), or even when

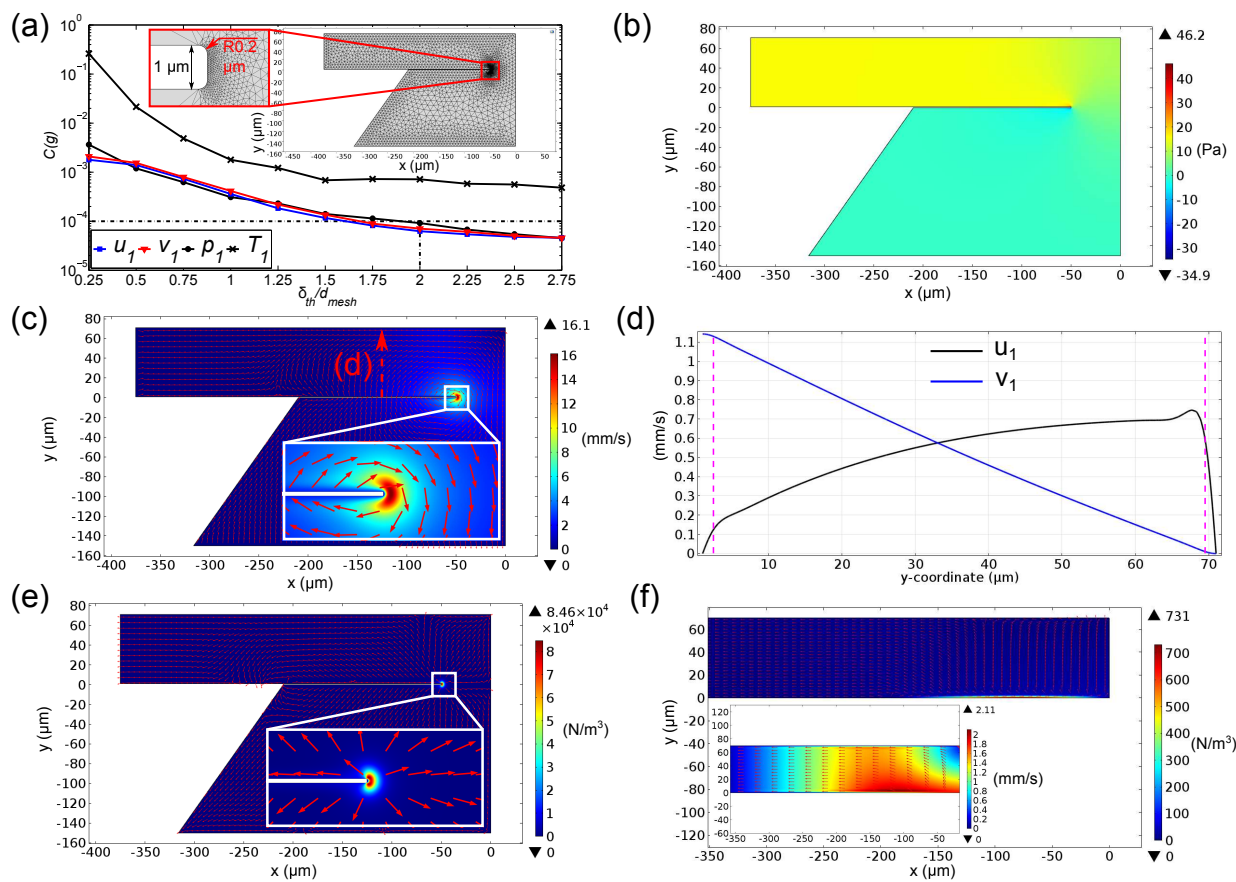


Fig. 4 COMSOL simulation results. (a) Mesh convergence parameter (lower is better) with an example mesh generated at $\delta_{th}/d_{mesh} = 0.1$. (b) Surface plot of the first-order pressure field. (c) Surface plot of the magnitude and the normalised arrow plot of \mathbf{v}_1 . (d) Plot of the components of \mathbf{v}_1 along the dashed red arrows located at the midpoint of the membrane's surface. (e) and (f) Surface plots of the body force magnitude and the field's normalised arrow plots created by the membrane with and without the hole, respectively. The magenta dashed lines in (d) indicate the viscous boundary layer. The inset in (f) shows the surface plot of the magnitude and the normalised arrow plot of \mathbf{v}_1 of a holeless membrane. The plots in (b)-(f) are produced at $\delta_{th}/d_{mesh} = 2$. The fine mesh at the hole's edge shown in the inset in (a) is kept unchanged for all δ_{th}/d_{mesh} ratio.

the flow is going through the hole (Fig. 5(h) and (i)).

As seen from Fig. 5(a), the chosen transition length for Eq. (3) is a conservative estimate of the transition from unmixed to mixed state. The true measurement would be at the location of the hole, which is rather difficult to obtain. In our analysis, such calculation of L_{mix} is chosen for consistency with previous studies.^{29,30,32}

3.2.2 Acoustic membranes with circular holes. Let us now characterise the mixing performance of the membranes with circular through holes. We can see from Fig. 6(a) and (b) that, for a given a/d ratio, both mixing efficiency and mixing time increase with decreasing Pe in most cases. The higher performing membranes, then, would have higher MI and lower t_{mix} . Most notably, the best circular membrane can achieve a mixing efficiency of 90% and time of 3 ms at 60

$\mu\text{l}/\text{min}$ flow rate ($Pe \approx 8333 \pm 3.5\%$), despite an extremely small portion of unmixed fluid remaining at the bottom wall in Fig. 6(ii) (see Video 2 in ESI). The critical role of hole is pronounced: even for the case of the smallest membrane width $a = 210 \mu\text{m}$ and $a/d = 3.5$ located in a $1000\text{-}\mu\text{m}$ -wide channel, a mixing index of 0.91 is observed, i.e. a 5-fold increase from a continuous, holeless membrane.

3.2.3 Acoustic membranes with holes of other geometries. Since the strength of the vortices and their symmetry around the bulk flow direction (both critical for efficient mixing as outlined in section 3.1) are strongly dependent on the properties of the through hole, it is logical to expect that mixing is dependent on the hole geometry. Fig. 7 analyses mixing for acoustic membranes with individual square-shaped and rectangular holes, as well as with a pair of square and circu-

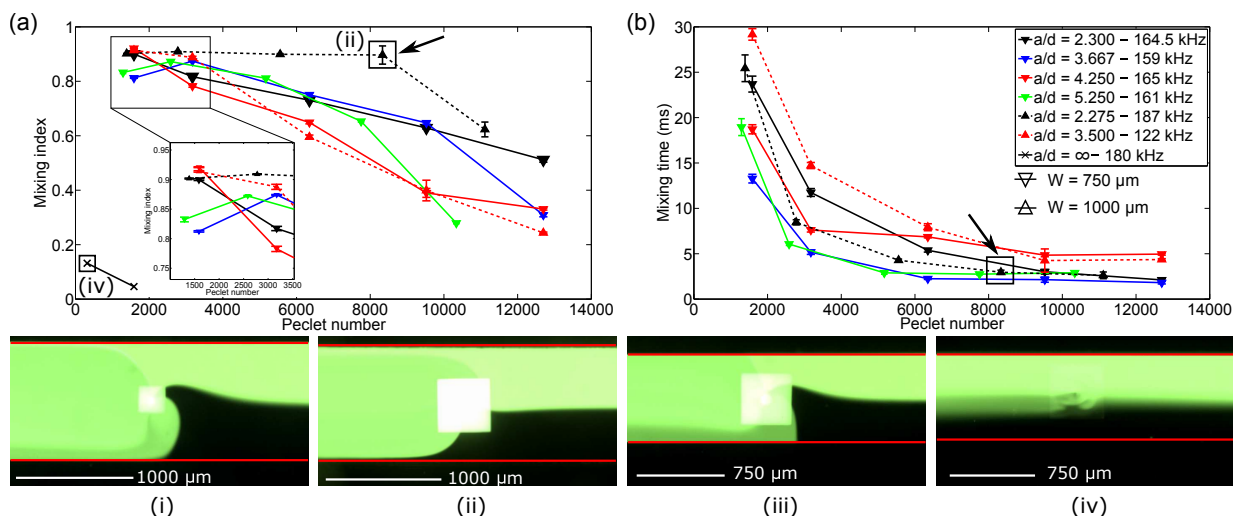


Fig. 6 Mixing characterisation of the membranes with circular holes. (a) and (b) show the mixing index and mixing time for various geometry ratios a/d at different Peclet numbers Pe , respectively. Mixing with the membrane with no hole ($a/d = \infty$) is performed in a $750\text{-}\mu\text{m}$ -wide channel at $Q = 2$ and $10 \mu\text{l}/\text{min}$, and its corresponding mixing time is not shown in (b). ∇ and \triangle markers represent the experiments with channel's width $W = 750$ and $1000 \mu\text{m}$, respectively. The arrow indicates the best circular mixer: $a/d = 2.275$, $MI = 0.90$ and $t_{mix} = 3$ ms. Errors are estimated by one standard error.

Table 1 Dimensions of the membranes with circular holes

a/d	a (μm)	d (μm)
2.300	230	100
3.667	440	120
4.250	425	100
5.250	420	80
2.275	455	200
3.500	210	60
∞	445	0

lar holes. We can see that a square hole can generate vortices whose centreline is aligned at 45° to the flow direction, resulting in higher mixing efficiency compared to a rectangular hole. Most notable is the membrane with a pair of square holes: mixing is achieved with $MI = 0.86$ and $t_{mix} = 4$ ms at $60 \mu\text{l}/\text{min}$ ($Pe \approx 8333 \pm 3.5\%$). While these values are lower than the best obtained with a circular hole membrane, the mixed fluid spans the entire channel width (Fig. 7(ii) compared to Fig. 6(ii)).

3.2.4 Acoustic membranes with air bubbles at the holes. One might think of covering the hole with an air/liquid interface to trap a bubble (a mechanism similar to the Lateral Cavity Acoustic Transducer⁵⁰), and see whether the membrane will behave similarly to a bubble mixer. This can be achieved by intentionally blocking the bottom outlet (originally intended to immerse the membrane in water) from the start. Interestingly, the resultant vortices are completely dif-

ferent from that of both the immersed acoustic membrane and the acoustic bubble.

Fig. 8 compares the streaming field, mixing performance and flow visualisation of a fully immersed membrane with those of a membrane covered with a bubble (henceforth referred to as the “bubble membrane”). In both cases, each hole generates two vortices, and the downstream pair is always stronger than the upstream one. The intensity graph shows that the exit flow is clearly divided into two regions of different mixing efficiency. Flow visualisation in Fig. 8(c) also confirms this division, albeit at a different frequency due to a clump of particles stuck at the upstream (right) hole. Note that the total flow rate of the immersed membrane is twice as high as the bubble one's.

On the other hand, the marked difference in the streaming field between the two cases can be observed even without flow visualisation. With the immersed membrane, the two holes are coupled, the incoming fluid passes over the upstream hole for the former. On the contrary, for the bubble membrane, the upstream hole's streaming field acts as a blockage. Mixing performance of the bubble membrane is also worse: its mixing index is lower than the immersed membrane that is being used at higher flow rates (0.78 at $5 \mu\text{l}/\text{min}$ compared to 0.81 at $10 \mu\text{l}/\text{min}$). This again emphasises the importance of the through hole of the membrane in mixing.

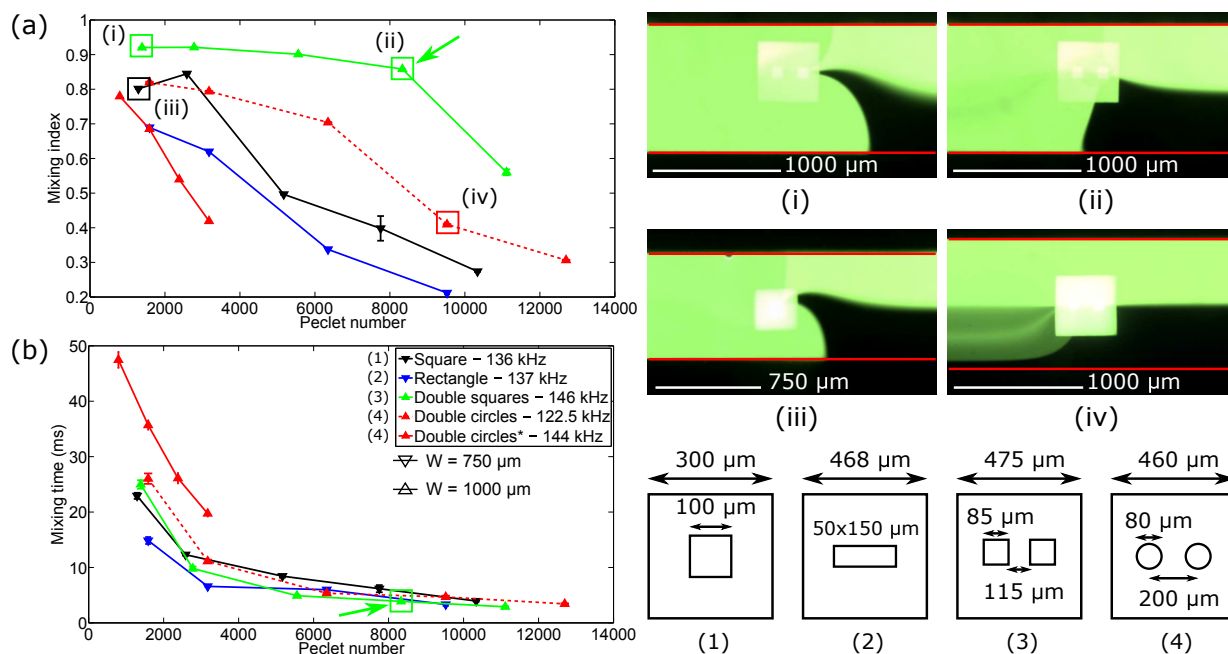


Fig. 7 Mixing characterisation of the membranes with different hole geometries. (a) and (b) show the mixing index and mixing time for a square hole and multiple holes at different Peclet numbers Pe . The device “Double circles*” uses the same membrane with two circular holes, except that the holes are covered by air bubbles instead of being completely immersed. This bubble device is tested at $Q = 5, 10, 15$ and $20 \mu\text{l}/\text{min}$, and will be analysed in the next section. \blacktriangledown and \blacktriangle markers represent the experiments with channel’s width $W = 750$ and $1000 \mu\text{m}$, respectively. The arrow indicates the best mixer in this case, the double square holes membrane, which can achieve $MI = 0.86$ and $t_{mix} = 4$ ms. Errors are estimated by one standard error.

4 Discussion

Microstreaming has previously been utilised to induce mixing, such as the bubble mixer¹³ or the oscillating sharp-edges.³² However, the nature of the streaming vortices generated by the acoustic membrane with a through hole is arguably more complicated.

It is well-known that streaming can be driven by an oscillating solid structure in a quiescent fluid, or equivalently a fixed structure in an oscillating fluid.⁴² With regards to its application in mixing, Huang *et al.*³² has shown that the streaming strength increases with decreasing equivalent spring stiffness. Applying this to our system, a membrane with the lowest stiffness (found to be the holeless membrane using ANSYS, which agrees with the equivalent stiffness result of a circular membrane with a circular hole⁵¹) for a given size a and thickness t should generate the strongest vortices. Yet, the resultant streaming field of this membrane is almost non-existent. Clearly, the vibration of the membrane alone is not a sufficient explanation for the observed mixing behaviour.

We have shown through simulations and experiments that the hole creates a discontinuity in the boundary conditions on the membrane, leading to a high velocity gradient. This in turn results in a strong body force field that drives the vortical

streaming field responsible for mixing.

While our numerical simulation neglects the fluid-structure coupling, it still gives a reasonably accurate description of the phenomenon. Firstly, the body force field concentrates around the hole’s edge (Fig. 4(e)), which arguably justifies why the streaming field is still observed for an offset hole. Secondly, the body force is a result of the first-order velocity gradient. Hence, when the fluid flows through the hole instead of above it, only the unperturbed velocity field \mathbf{v}_0 changes, leaving \mathbf{v}_0 and thus \mathbf{F} unchanged. (Only the streaming field pattern \mathbf{v}_s is expected to change.) And thirdly, the “bubble membrane” is likely to have a different deflection mode ($w(x)$ used in Eq. (10c)), and there is no longer coupling of fluid on both sides of the membrane. Consequently, a different streaming behaviour is observed compared to that of an immersed membrane. As to why the vortices appear different from that of a bubble mixer, we can see that the edges of the bubbles in the bubble membrane are not fixed, instead they are vibrating together with the edges of the membrane’s holes. This leads to a different set of boundary conditions for the bubble, and as a result produces a dissimilar behaviour.

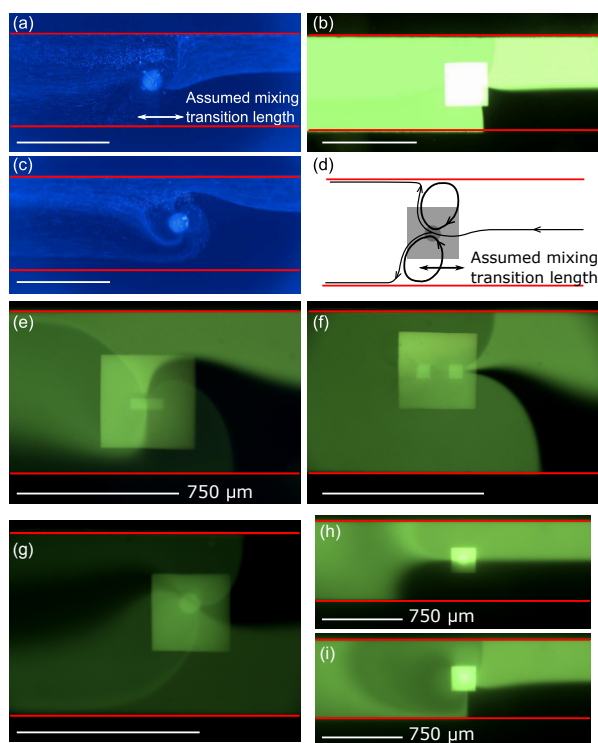


Fig. 5 Flow visualisation and mixing of the acoustic membrane at $10 \mu\text{l}/\text{min}$. (a) Streaming pattern at 224 kHz. (b) Mixing at 187 kHz. (c) Streaming pattern at 235 kHz. (d) Schematic of the resultant vortices around the membrane. (e) Mixing of a membrane with a rectangular hole at 137 kHz. (f) Mixing of a membrane with two square holes at 146 kHz. (g) Mixing with a membrane with a hole offset from the centre at 228 kHz. (h) and (i) show the case when fluid flows through the membrane's hole when it is turned OFF and ON, respectively, at 136 kHz. The membrane in (a), (b) and (c) has $a = 455 \mu\text{m}$ and $d = 200 \mu\text{m}$; the membrane used in (g) has $a = 425 \mu\text{m}$ and $d = 120 \mu\text{m}$; and the one in (h) and (i) has $a = 230 \mu\text{m}$ and $d = 100 \mu\text{m}$. All scale bars are $1000 \mu\text{m}$ unless otherwise specified.

5 Conclusions

We have presented a novel approach for microfluidic mixing: the acoustic membrane mixer. The system uses robust microfabricated structures with precisely defined geometries to generate a highly controllable streaming field. Importantly, it has been shown that the introduction of geometric singularities (such as circular or square-shaped through holes of varying dimensions) within the vibrating structures do significantly alter the induced streaming and may hence be used to further enhance the mixing efficiency. The membrane is numerically modelled to show that the volume force due to the first-order velocity gradient, which is responsible for driving the streaming vortices, is 2 orders of magnitude higher when the hole is introduced. This agrees with our hypothesis that the hole

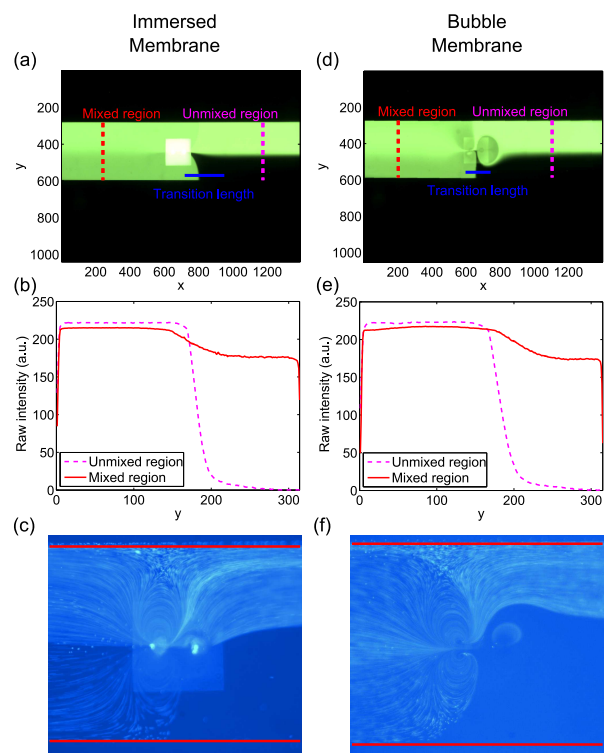


Fig. 8 Different streaming patterns observed when the holes are covered by air bubbles in a $1000\text{-}\mu\text{m}$ -wide channel. (a) and (b) show mixing of a fully immersed membrane with double circular holes at $10 \mu\text{l}/\text{min}$ and 122.5 kHz . (c) Visualisation of the flow caused by the immersed membrane $10 \mu\text{l}/\text{min}$ and 107.7 kHz . (d), (e) and (f) show mixing performance and flow visualisation of the bubble membrane at $5 \mu\text{l}/\text{min}$ and 144 kHz . For the immersed membrane: $MI = 0.81$ and $t_{\text{mix}} = 26.4 \text{ ms}$; for the bubble membrane: $MI = 0.78$ and $t_{\text{mix}} = 47.3 \text{ ms}$. All x and y coordinates in (a)-(e) are in pixels.

significantly increases the velocity gradient by introducing a discontinuity in the boundary conditions.

Experiments show that the acoustic membrane's mixing efficiency can reach 90% in a surprisingly fast 3 ms at a flow rate of $60 \mu\text{l}/\text{min}$ ($Pe \approx 8333 \pm 3.5\%$). Various geometries of the holes have also been tested, and we observe that a membrane with a couple of square holes can mix fluid at 4 ms and 86% efficiency at $Pe \approx 8333 \pm 3.5\%$. Additionally, investigations on the effects of having the holes covered by air bubbles yield interesting results. The streaming pattern is markedly different: the bubbles do not couple with each other as observed in the case of an immersed membrane, i.e. fluid only flows through the vortices generated by one bubble, reducing the mixing performance. Our mixer is a potential candidate for microfluidic applications that require mixing such as nanoparticles synthesis.

6 Acknowledgements

This work was performed in part at the Melbourne Centre for Nanofabrication (MCN) in the Victorian Node of the Australian National Fabrication Facility (ANFF). The authors would like to thank Prashant Agrawal for helpful discussions of the numerical methods and the Australian Research Council (No. DP110104010) for their kind support of this research.

References

- 1 K. F. Jensen, S. L. Firebaugh, A. J. Franz, D. Quiram, R. Srinivasan and M. A. Schmidt, *Micro Total Analysis Systems* 98, 1998, pp. 463–468.
- 2 L. Pollack, M. W. Tate, N. C. Darnton, J. B. Knight, S. M. Gruner, W. A. Eaton and R. H. Austin, *Proc. Natl. Acad. Sci. U.S.A.*, 1999, **96**, 10115–10117.
- 3 R. Karnik, F. Gu, P. Basto, C. Cannizzaro, L. Dean, W. Kyei-Manu, R. Langer and O. C. Farokhzad, *Nano Lett.*, 2008, **8**, 2906–2912.
- 4 N. M. Belliveau, J. Huft, P. J. Lin, S. Chen, A. K. Leung, T. J. Leaver, A. W. Wild, J. B. Lee, R. J. Taylor, Y. K. Tam *et al.*, *Mol Ther Nucleic Acids*, 2012, **1**, e37.
- 5 J.-M. Lim and R. Karnik, *Nanomedicine*, 2014, **9**, 1113–1116.
- 6 J. M. Ottino and S. Wiggins, *Philos Trans A Math Phys Eng Sci*, 2004, **362**, 923–935.
- 7 J. B. Knight, A. Vishwanath, J. P. Brody and R. H. Austin, *Phys. Rev. Lett.*, 1998, **80**, 3863.
- 8 A. D. Stroock, S. K. Dertinger, A. Ajdari, I. Mezić, H. A. Stone and G. M. Whitesides, *Science*, 2002, **295**, 647–651.
- 9 H. Wang, P. Iovenitti, E. Harvey and S. Masood, *Smart Mater. Struct.*, 2002, **11**, 662.
- 10 C.-P. Jen, C.-Y. Wu, Y.-C. Lin and C.-Y. Wu, *Lab Chip*, 2003, **3**, 77–81.
- 11 Y. Z. Liu, B. J. Kim and H. J. Sung, *Int. J. Heat Fluid Flow*, 2004, **25**, 986–995.
- 12 B. He, B. J. Burke, X. Zhang, R. Zhang and F. E. Regnier, *Anal. Chem.*, 2001, **73**, 1942–1947.
- 13 R. H. Liu, J. Yang, M. Z. Pindera, M. Athavale and P. Grodzinski, *Lab Chip*, 2002, **2**, 151–157.
- 14 C.-H. Tai, R.-J. Yang, M.-Z. Huang, C.-W. Liu, C.-H. Tsai and L.-M. Fu, *Electrophoresis*, 2006, **27**, 4982–4990.
- 15 Y. Wang, J. Zhe, B. T. Chung and P. Dutta, *Microfluid Nanofluidics*, 2008, **4**, 375–389.
- 16 S. Oberti, A. Neild and T. W. Ng, *Lab Chip*, 2009, **9**, 1435–1438.
- 17 A. Neild, T. W. Ng, G. J. Sheard, M. Powers and S. Oberti, *Sens. Actuators, B*, 2010, **150**, 811–818.
- 18 N.-T. Nguyen and Z. Wu, *J. Micromech. Microeng.*, 2005, **15**, R1.
- 19 C.-Y. Lee, C.-L. Chang, Y.-N. Wang and L.-M. Fu, *Int J Mol Sci*, 2011, **12**, 3263–3287.
- 20 M. Wiklund, C. Günther, R. Lemor, M. Jäger, G. Fuhr and H. M. Hertz, *Lab Chip*, 2006, **6**, 1537–1544.
- 21 T. Laurell, F. Petersson and A. Nilsson, *Chem. Soc. Rev.*, 2007, **36**, 492–506.
- 22 R. Walker, I. Gralinski, K. K. Lay, T. Alan and A. Neild, *Appl. Phys. Lett.*, 2012, **101**, 163504.
- 23 P. Rogers and A. Neild, *Lab Chip*, 2011, **11**, 3710–3715.
- 24 D. J. Collins, T. Alan and A. Neild, *Lab Chip*, 2014, **14**, 1595–1603.
- 25 X. Ding, Z. Peng, S.-C. S. Lin, M. Geri, S. Li, P. Li, Y. Chen, M. Dao, S. Suresh and T. J. Huang, *Proc. Natl. Acad. Sci. U.S.A.*, 2014, **111**, 12992–12997.
- 26 H. V. Phan, M. Şeşen, T. Alan and A. Neild, *Appl. Phys. Lett.*, 2014, **105**, 193507.
- 27 K. Sritharan, C. Strobl, M. Schneider, A. Wixforth and Z. v. Guttenberg, *Appl. Phys. Lett.*, 2006, **88**, 054102.
- 28 S. S. Wang, Z. J. Jiao, X. Y. Huang, C. Yang and N. T. Nguyen, *Microfluid Nanofluidics*, 2009, **6**, 847–852.
- 29 D. Ahmed, X. Mao, J. Shi, B. K. Juluri and T. J. Huang, *Lab Chip*, 2009, **9**, 2738–2741.
- 30 D. Ahmed, X. Mao, B. K. Juluri and T. J. Huang, *Microfluid Nanofluidics*, 2009, **7**, 727–731.
- 31 M. C. Jo and R. Guldiken, *Sens. Actuators, A*, 2013, **196**, 1–7.
- 32 P.-H. Huang, Y. Xie, D. Ahmed, J. Rufo, N. Nama, Y. Chen, C. Y. Chan and T. J. Huang, *Lab Chip*, 2013, **13**, 3847–3852.
- 33 A. Ozcelik, D. Ahmed, Y.-L. Xie, N. Nama, Z. Qu, A. A. Nawaz and T. J. Huang, *Anal. Chem.*, 2014.
- 34 H. Jagannathan, G. G. Yaralioglu, A. S. Ergun, F. Degertekin and B. Khuri-Yakub, *Ultrasonics Symposium*, 2001 IEEE, 2001, pp. 859–862.
- 35 G. G. Yaralioglu, I. O. Wygant, T. C. Marentis and B. T. Khuri-Yakub, *Anal. Chem.*, 2004, **76**, 3694–3698.
- 36 J. Creemer, F. Santagata, B. Morana, L. Mele, T. Alan, E. Iervolino, G. Pandraud and P. Sarro, *Micro Electro Mechanical Systems (MEMS)*, 2011 IEEE 24th International Conference on, 2011, pp. 1103–1106.
- 37 T. Yokosawa, T. Alan, G. Pandraud, B. Dam and H. Zandbergen, *Ultramicroscopy*, 2012, **112**, 47–52.
- 38 T. Alan, T. Yokosawa, J. Gaspar, G. Pandraud, O. Paul, F. Creemer, P. M. Sarro and H. W. Zandbergen, *Appl. Phys. Lett.*, 2012, **100**, 081903.
- 39 T.-D. Luong, V.-N. Phan and N.-T. Nguyen, *Microfluidics and nanofluidics*, 2011, **10**, 619–625.
- 40 A. Hashmi and J. Xu, *J Lab Autom*, 2014, **19**, 488–491.
- 41 N.-T. Nguyen and R. M. White, *Ultrasonics, Ferroelectrics, and Frequency Control*, *IEEE Transactions on*, 2000, **47**, 1463–1471.
- 42 W. Nyborg, *Physical acoustics*, 1965, **2**, 265.
- 43 P. Agrawal, P. S. Gandhi and A. Neild, *Physical Review Applied*, 2014, **2**, 064008.
- 44 C. Devendran, I. Gralinski and A. Neild, *Microfluid Nanofluidics*, 2014, 1–12.
- 45 P. M. Morse and K. U. Ingard, *Theoretical acoustics*, Princeton university press, 1968.
- 46 P. B. Muller, R. Barnkob, M. J. H. Jensen and H. Bruus, *Lab Chip*, 2012, **12**, 4617–4627.
- 47 A. W. Leissa, *Vibration of plates*, Dtic document technical report, 1969.
- 48 R. Moroney, R. White and R. Howe, *Applied physics letters*, 1991, **59**, 774–776.
- 49 L. Pan, T. Ng, G. Liu, K. Lam and T. Jiang, *Sensors and Actuators A: Physical*, 2001, **93**, 173–181.
- 50 A. R. Tovar and A. P. Lee, *Lab Chip*, 2009, **9**, 41–43.
- 51 S. Timoshenko and S. Woinowsky-Krieger, *Theory of plates and shells*, McGraw-Hill New York, 1959, vol. 2.